

Supplementary Materials for  
**A spatiotemporal complexity architecture of human brain activity**

Stephan Krohn *et al.*

Corresponding author: Stephan Krohn, [stephan.krohn@charite.de](mailto:stephan.krohn@charite.de); Carsten Finke, [carsten.finke@charite.de](mailto:carsten.finke@charite.de)

*Sci. Adv.* **9**, eabq3851 (2023)  
DOI: 10.1126/sciadv.abq3851

**The PDF file includes:**

Figs. S1 to S14  
Legend for movie S1

**Other Supplementary Material for this manuscript includes the following:**

Movie S1

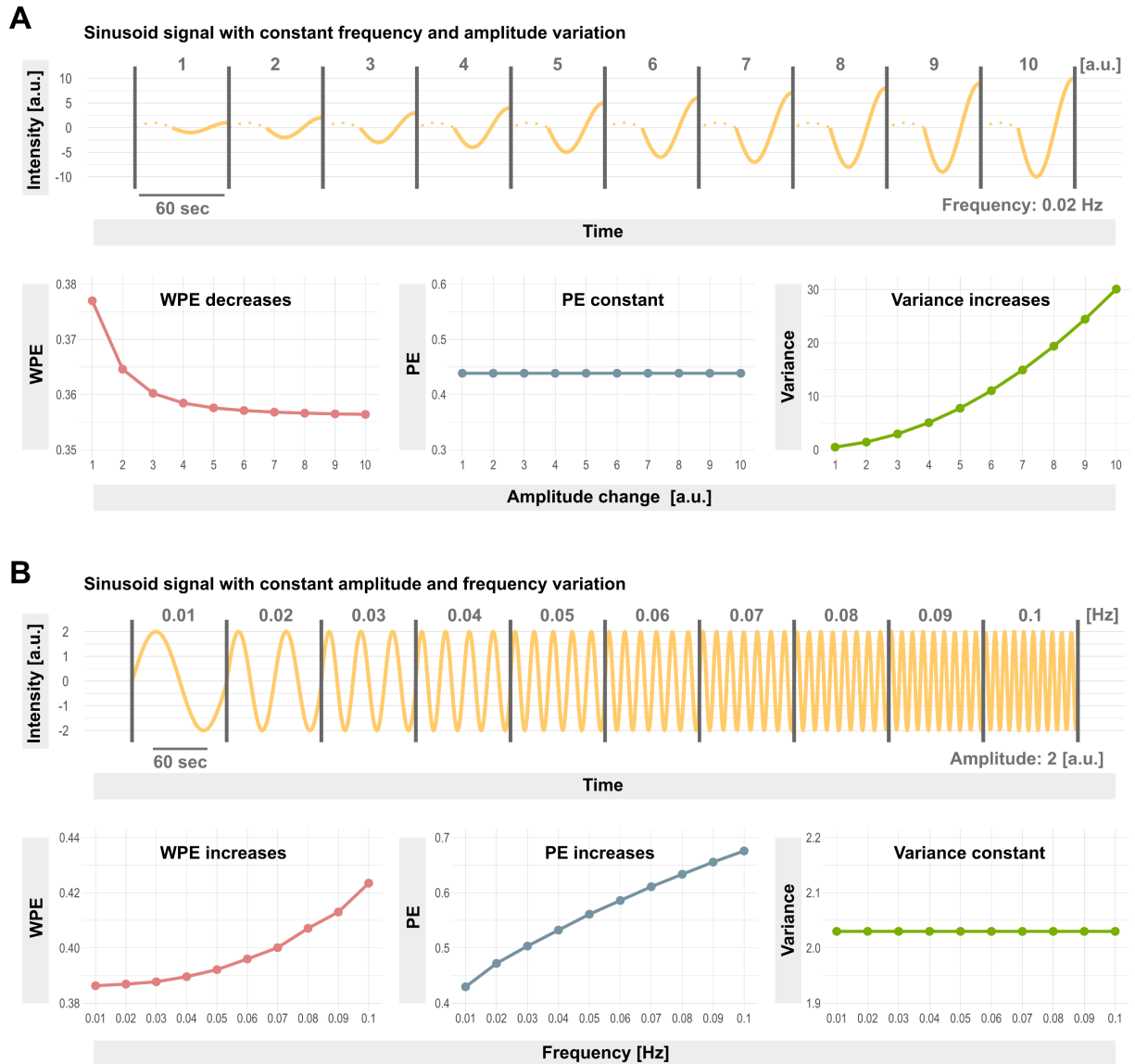


**Fig. S1. Weighted permutation entropy reflects amplitude and frequency variation that remains undetected when considering only pattern diversity or signal variance alone. (A)** Simulated sinusoid signal with constant frequency in the range of real BOLD signals (0.02 Hz) and with systematically increasing amplitude variation that results in changes of weighted permutation entropy (WPE) and amplitude variance, whereas pattern diversity alone (permutation entropy, PE) remains identical. **(B)** Simulated sinusoid signal with constant amplitude and systematically increasing frequency variation that results in changes of weighted permutation entropy (WPE) and pattern diversity (PE), while signal variance remains unchanged. Note that WPE values monotonically increase with the higher frequency content, reaching about 0.42 normalized bits at 0.1 Hz (identical to the applied low-pass filter settings in BOLD preprocessing), consistent with the empirically observed upper limit of the complexity timeseries derived from real BOLD signals (Fig. 1A, online repository <https://osf.io/mr8f7>, and Fig. S3 and S4).

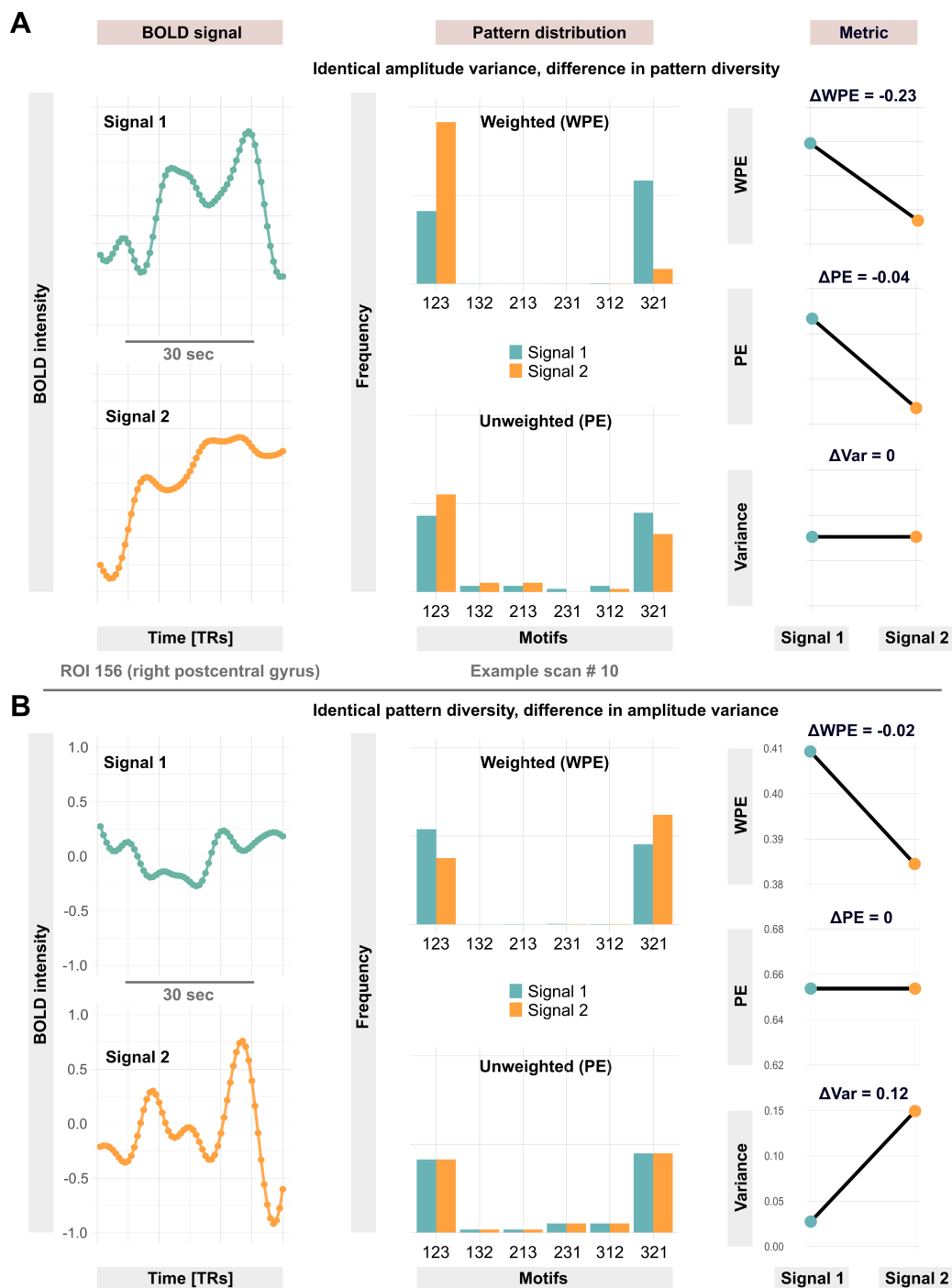


**Fig. S2. Weighted permutation entropy tracks BOLD signal dynamics that remain undetected when considering only pattern diversity or signal variance alone. (A)** BOLD signals with identical amplitude variance but varying pattern diversity (permutation entropy, PE). **(B)** BOLD signals with identical pattern diversity but varying amplitude variance. All signal snippets correspond to non-overlapping BOLD windows from the right postcentral gyrus of a representative resting-state recording. Columns show BOLD signals (left), the associated variance-weighted pattern distributions (middle), and the change in signal metrics (right).

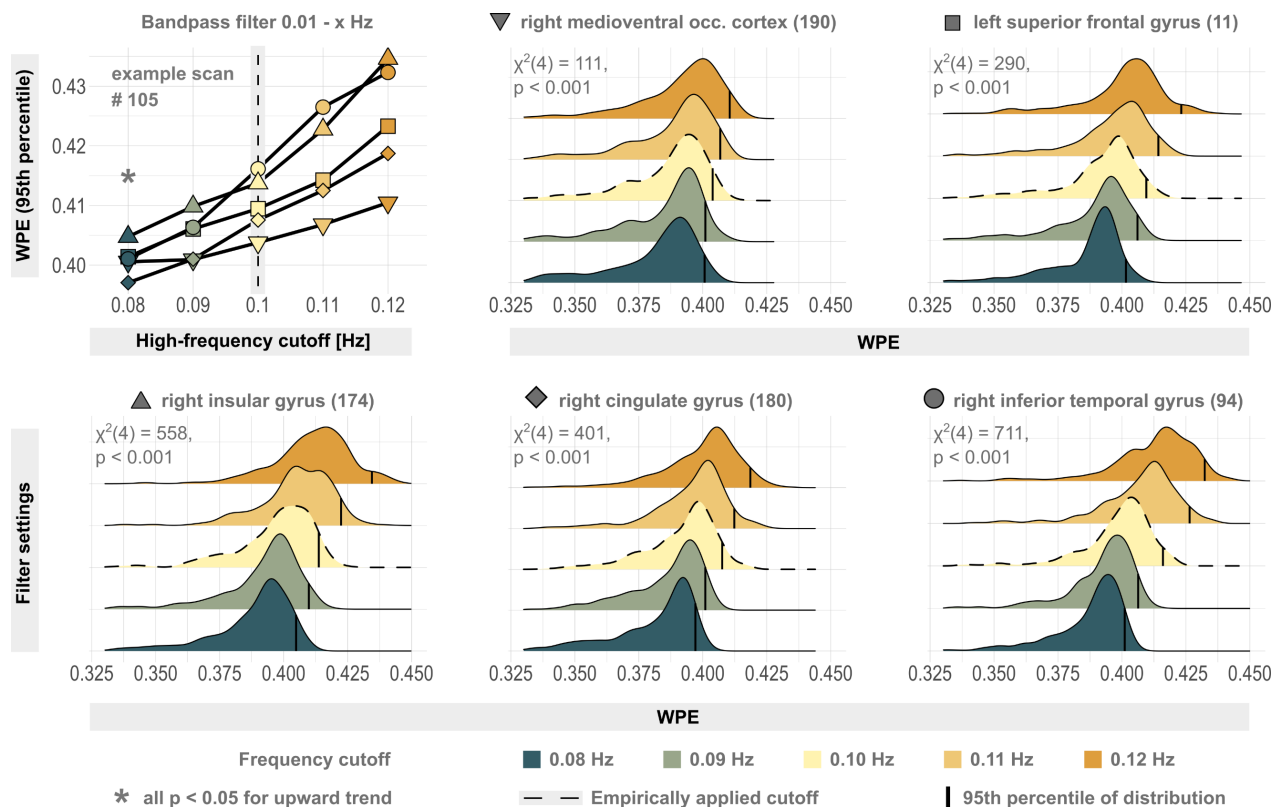


**Fig. S3. Upper-frequency content scales the distribution of weighted permutation entropy.** The upper left panel shows the 95th percentile of weighted permutation entropy (WPE) values from five randomly selected ROIs over different bandpass filter settings in a representative resting-state dataset. Brainnetome IDs of regions are given in brackets. In line with the frequency-sensitivity in pure sine signals (Fig. S1), systematic variation of the high-frequency cutoff gradually scales the upper limits of WPE values, which becomes apparent as a significant monotonic upward trend in nonparametric Mann-Kendall tests and a systematic right-shift of the WPE distributions for individual regions. Note, however, that the heavy left tails (corresponding to complexity drops, see Fig. 6A) are unaffected by the scaling of the distributions. For the applied low-pass cutoff of 0.1 Hz in the main text (dashed lines), maximum WPE values converge around 0.42 normalized bits in both simulated and real signals, in line with the empirically observed upper limit of individual complexity timeseries (Fig. 1A and 6A, online repository <https://osf.io/mr8f7>, and Fig. S4).



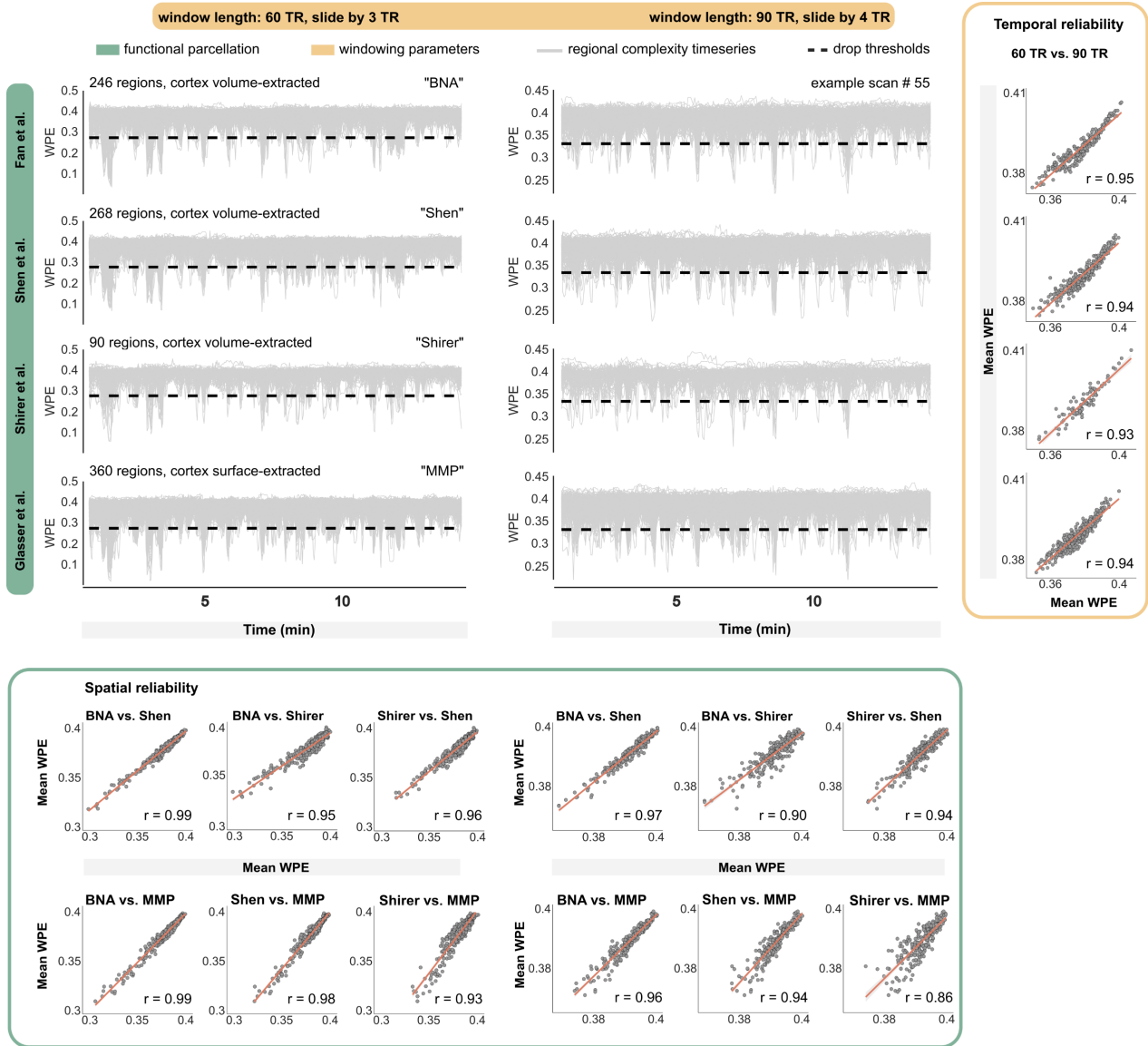


**Fig. S4. Resting-state complexity dynamics are robust across functional parcellation granularity, windowing parameters, and timeseries extraction methods.** Time-resolved weighted permutation entropy (WPE) from an exemplary HCP scan (see Fig. 1A). The data were parcellated with three common volumetric brain atlases of varying spatial granularity —after Fan et al. (63), after Shen et al. (64), and after Shirer et al. (65)— as well as with the MMP atlas after Glasser et al. (66), in which subcortical timeseries are extracted volumetrically but extraction of cortical signals is surface-based. Furthermore, different windowing parameters for computing WPE timeseries are applied (60 TRs sliding by 3 TRs, and 90 TRs sliding by 4TRs). Spatial reliability is calculated as the correlation over time points for every combination of functional atlases, and temporal reliability is computed as the correlation of mean WPE values of every ROI for the two windowing parameters. Results in the main text are based on the Brainnetome atlas (BNA) after Fan et al. (63) and 60 TR windows sliding to the next window by 3 TRs (upper left panel here).

# Spatial topology of signal complexity

■ medial wall / area not covered by atlas

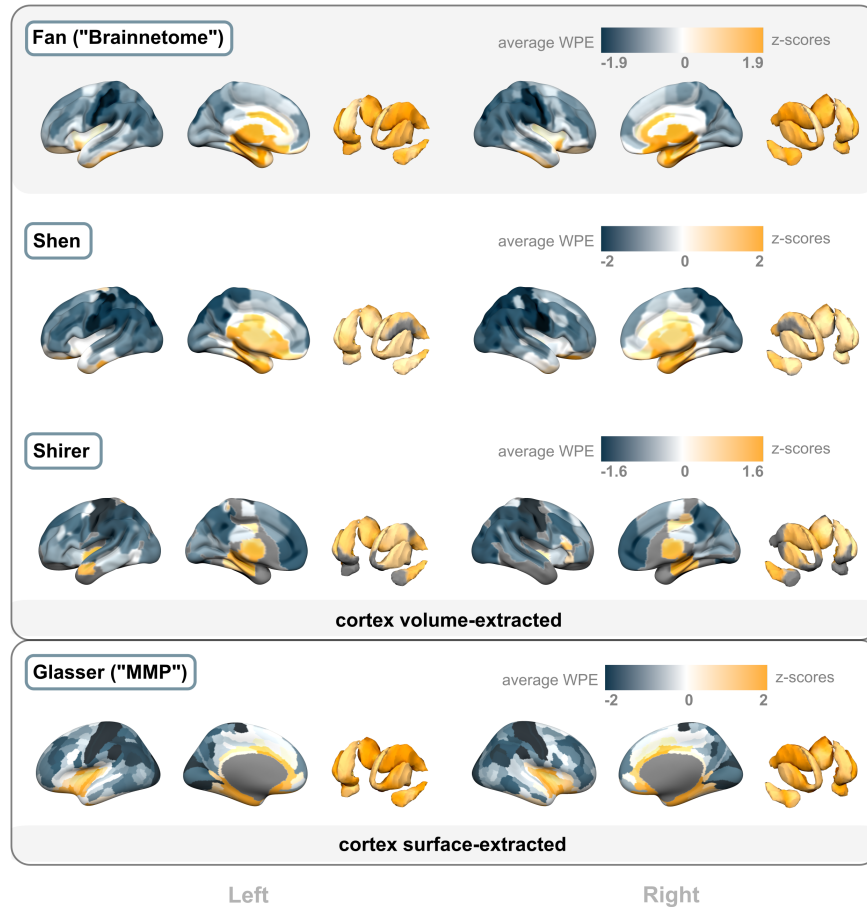


**Fig. S5. The spatial topology of signal complexity is robust across functional parcellation granularity and timeseries extraction methods.** Spatial distribution of weighted permutation entropy averaged across participants. The same four functional brain atlases as in Fig. S4 were used: the Brainnetome atlas after Fan et al. (63), the atlases after Shen et al. (64) and Shirer et al. (65), and the MMP atlas after Glasser et al. (66). The results from the main text are based on the Brainnetome atlas (gray background). The divergence between subcortical regions (high complexity) and cortex, especially in pericentral areas (low complexity), is equivalently observed with two volume-based atlases of higher (Shen) and lower (Shirer) spatial granularity as well as in surface-based extraction of cortical timeseries (Glasser).

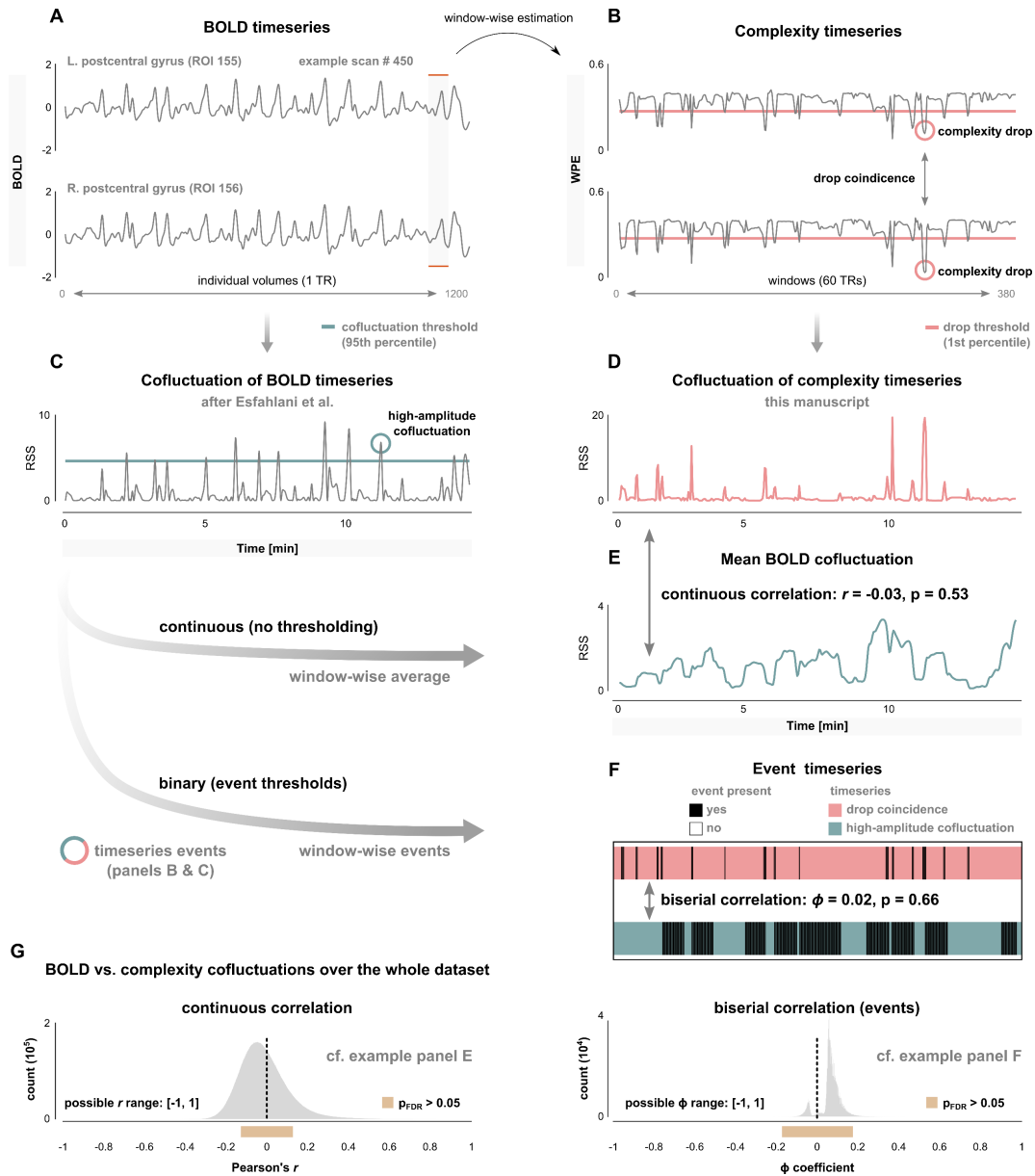


**Fig. S6. Complexity dynamics are distinct from BOLD signal confluctuations derived from edge timeseries.** (A) Exemplary BOLD timeseries of two brain regions. (B) The corresponding complexity timeseries of these signals over BOLD windows, as in Fig. 1A. Illustration of a drop coincidence between these regions (see Fig. 1C). (C) Cofluctuation of the BOLD timeseries in panel A, as defined by Esfahlani et al. (30). Illustration of high-amplitude confluctuation events. Following Esfahlani and colleagues, the event threshold was set to the 95<sup>th</sup> percentile of the root sum square (RSS) timeseries. (D) Cofluctuation of the complexity timeseries in panel B, computed in analogy to BOLD confluctuations. (E) Mean BOLD confluctuation amplitude in panel C over windows. Continuous correlation between BOLD confluctuation amplitude and complexity confluctuation amplitude. (F) Binary event timeseries showing if a drop coincidence was present in a given window (upper row) and if a high-amplitude BOLD confluctuation was present in a given window (lower row). Biserial correlation between the two event timeseries. (G) Continuous and biserial correlations between BOLD confluctuations and complexity confluctuations over the whole dataset.

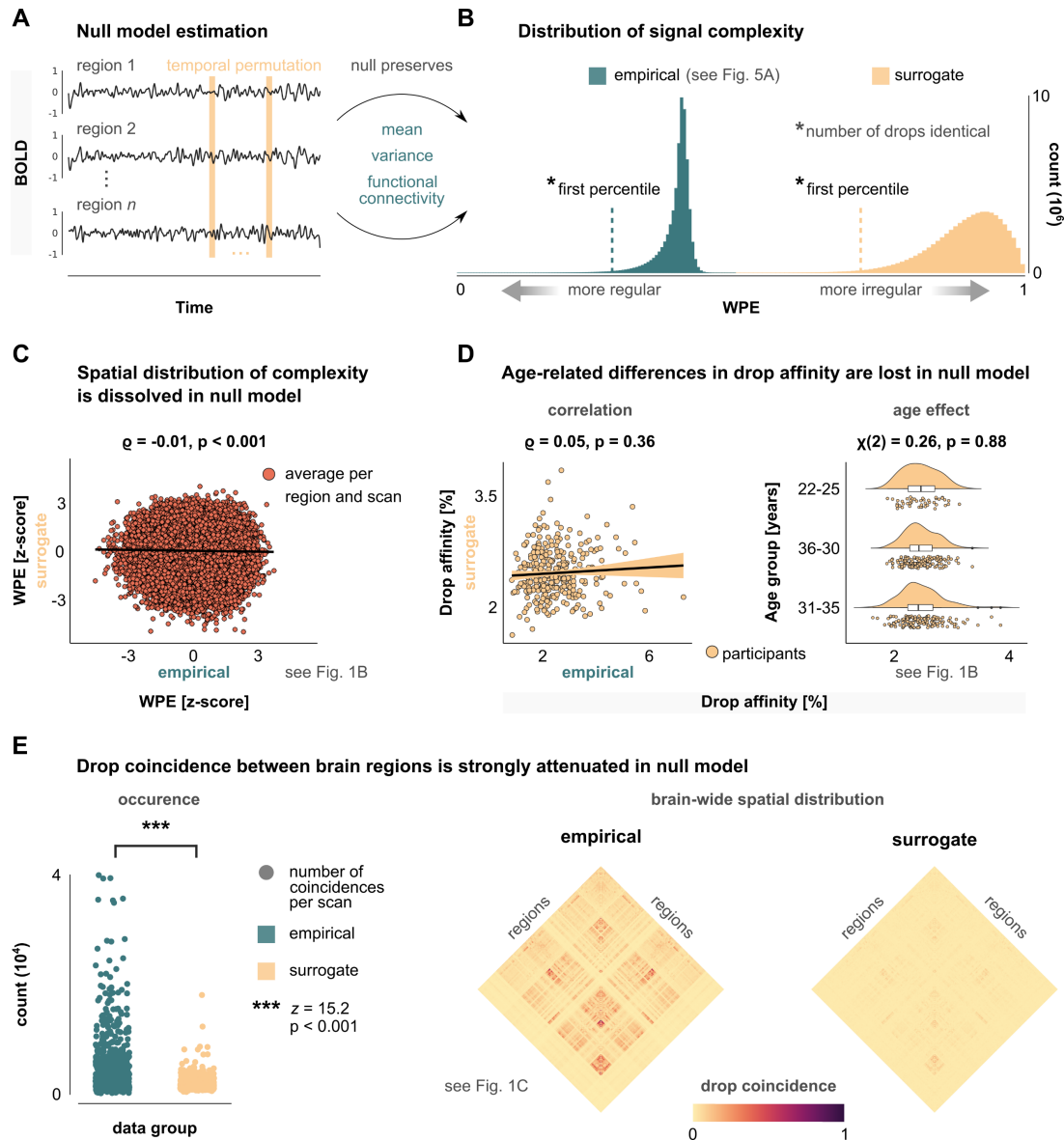


**Fig. S7. Spatial, temporal, and interindividual effects of complexity dynamics are dissolved under a null model of temporal dependency.** (A) Illustration of the null model estimation. BOLD timeseries were subjected to a temporal permutation approach that preserves signal means, amplitude variance, and functional connectivity but dissolves the temporal structure of the timeseries. The permutation was applied homogeneously over regions and scans. (B) Distribution of signal complexity in the empirical and the surrogate data. Note that since complexity drops are defined as instances below the first percentile of this distribution, the absolute number of drops are identical in empirical and surrogate data. (C) The spatial distribution of signal complexity across brain regions in surrogate vs. empirical data. Points represent the z-scored average signal complexity of individual brain regions for each scan in the main dataset ( $n=684$ ). (D) Participant-wise affinity for complexity drops in empirical vs. surrogate data (left) and over age groups (right), as in Fig. 1B. (E) Drop coincidences between brain regions in empirical and surrogate data. The left panel compares the number of coincidences per scan (rank sum test). The right panels show the distribution of drop coincidence among brain regions, where the matrix for the empirical data corresponds to the points displayed in Fig. 1C. While these matrices display average values across all scans, spatial drop coincidence patterns were also strongly dissolved on the level of individual scans (correlation in empirical vs. surrogate data:  $p = 0.04 \pm 0.03, n=684$  scans).

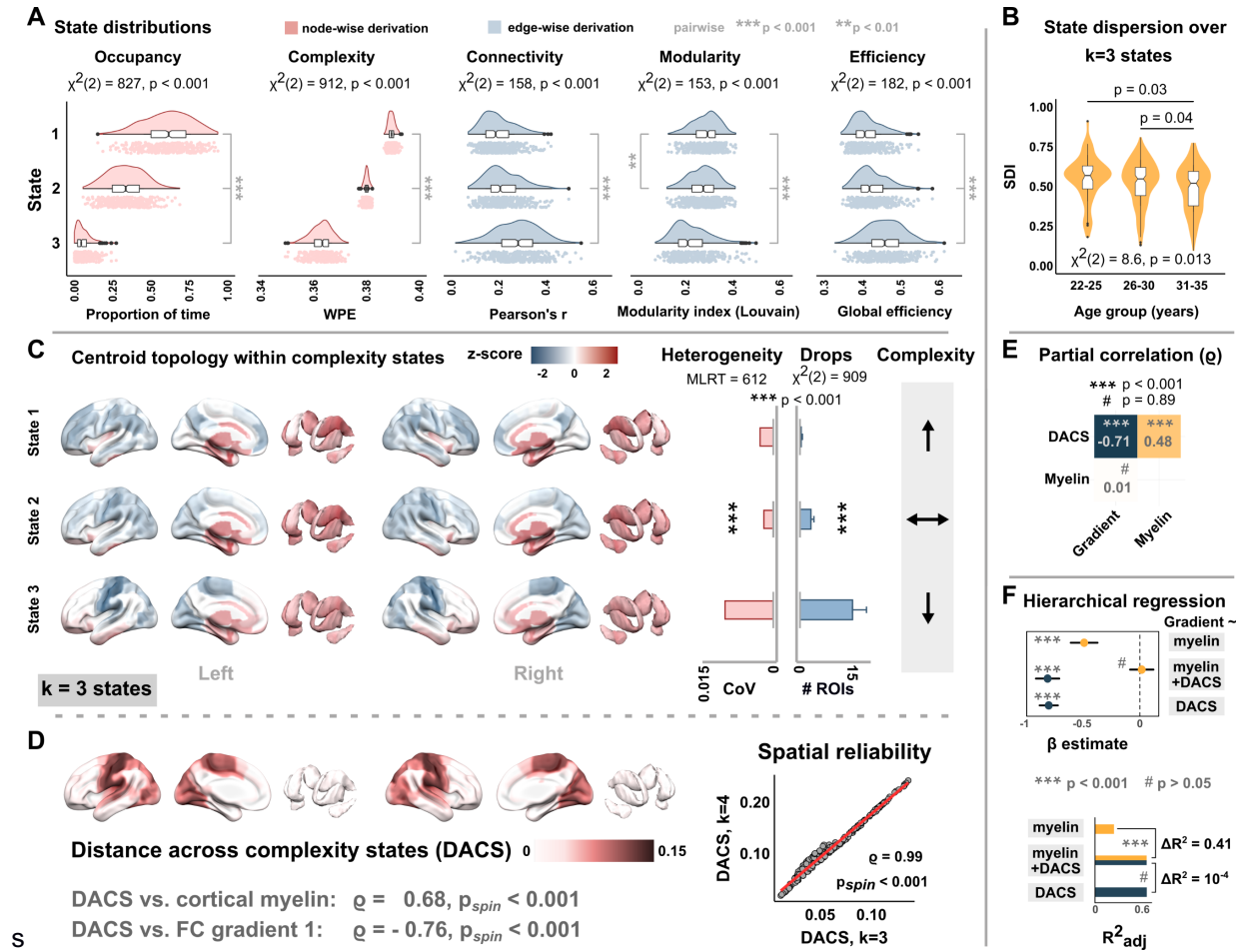


**Fig. S8. Validation analyses for k=3 expected complexity states.** (A) State-wise distributions of occupancy, signal complexity, FC strength, network modularity, and global efficiency. (B) Age-related reduction of state exploration. (C) Spatial topology, heterogeneity, and state-wise drop distribution over complexity states. (D) Spatial topology, and spatial reliability of the distance across complexity states (DACS) compared to k=4 expected complexity states. (E) Partial correlation between the DACS, myelin, and the unimodal-to-transmodal connectivity gradient loadings. (F) Hierarchical regression on the gradient loadings with myelin content and the DACS as explanatory variables. All results closely follow the findings reported in Fig. 3 and 4 of the main text.

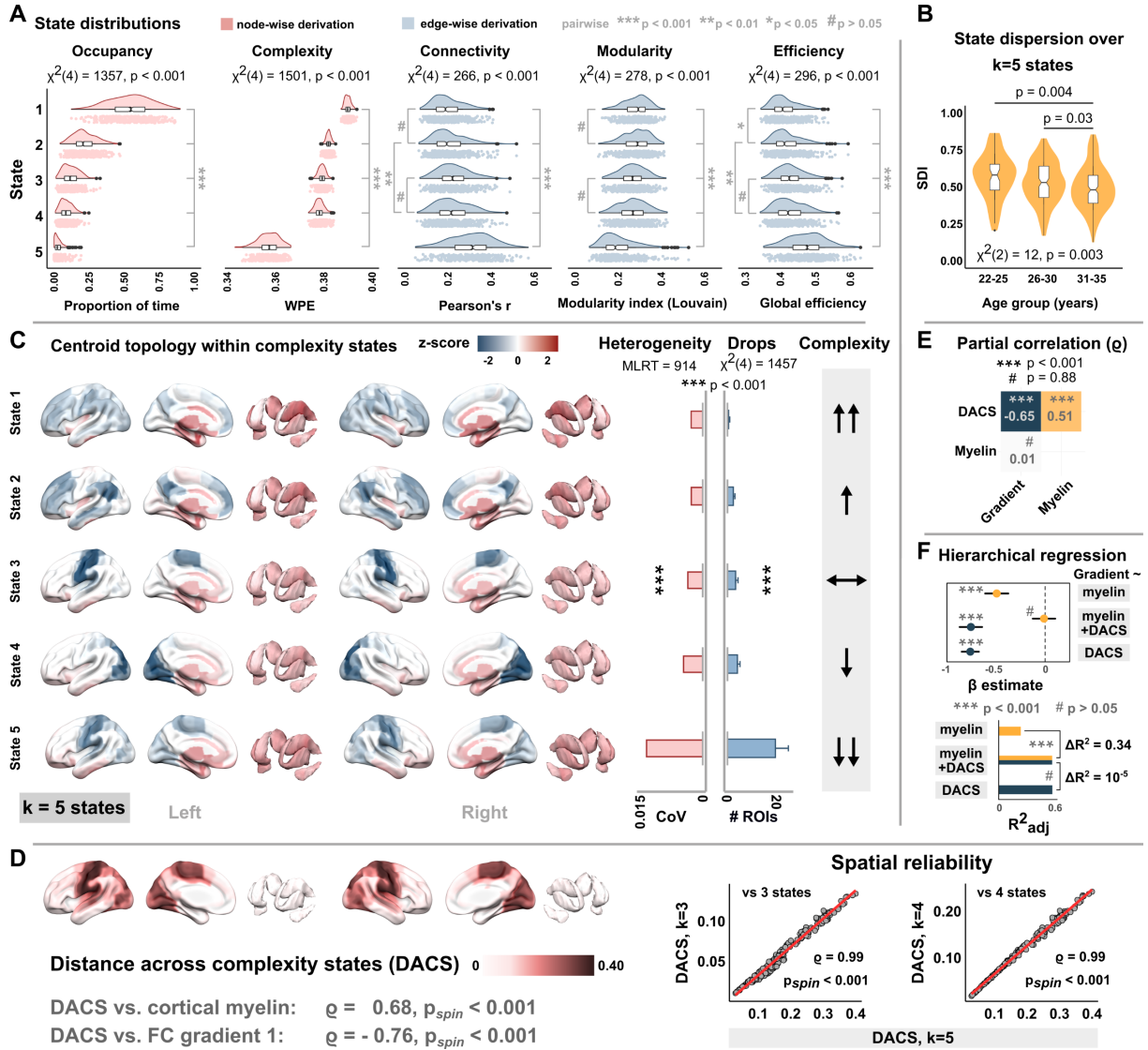


**Fig. S9. Validation analyses for k=5 expected complexity states.** (A) State-wise distributions of occupancy, signal complexity, FC strength, network modularity, and global efficiency. (B) Age-related reduction of state exploration. (C) Spatial topology, heterogeneity, and state-wise drop distribution over complexity states. (D) Spatial topology, and spatial reliability of the distance across complexity states (DACS) compared to k=4 and k=3 expected complexity states. (E) Partial correlation between the DACS, myelin, and the unimodal-to-transmodal connectivity gradient loadings. (F) Hierarchical regression on the gradient loadings with myelin content and the DACS as explanatory variables. As for k=3 expected complexity states (Fig. S8), results closely follow the findings reported in Fig. 3 and 4 of the main text.



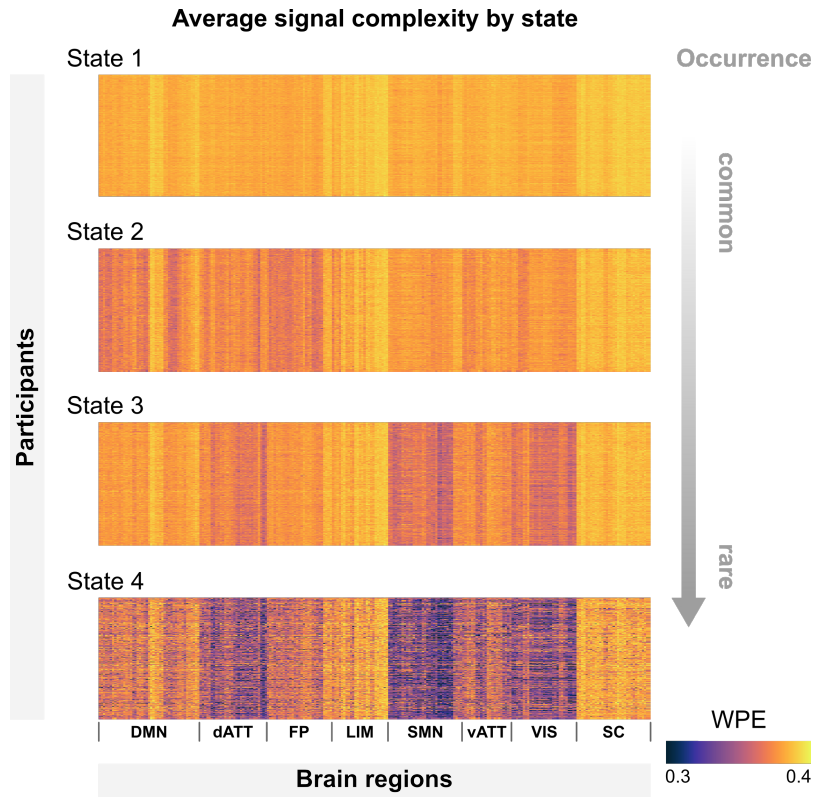


**Fig. S10. Distribution of signal complexity by participant and brain region across complexity states.** The carpet plots show the mean weighted permutation entropy (WPE) values for a brain region (columns, ordered by resting-state networks) of individual participants (rows) in each of the four identified states.

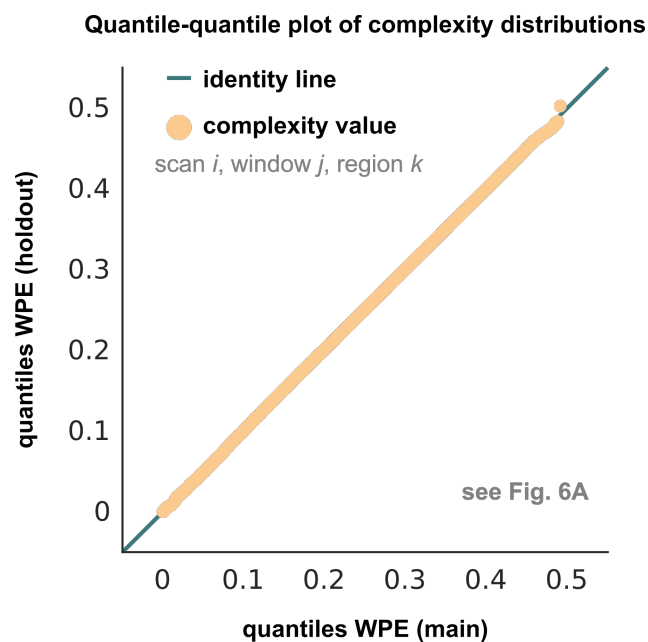


**Fig. S11. Quantile-quantile plot of complexity distributions in main and holdout data.** The plot shows the close correspondence between the distributions of weighted permutation entropy in the main and holdout data with ~64 million instances each (scans x windows x regions), as shown in Figure 6A of the main text.



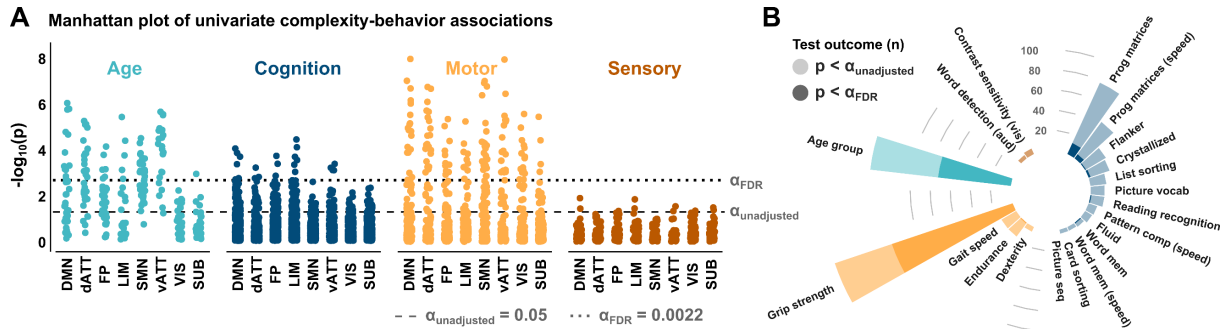


**Fig. S12. Univariate complexity-behavior associations over individual scores.** (A) Manhattan plot of negative log p-values for nonparametric correlation tests between behavioral variables and regional WPE values (dashed line: unadjusted alpha-level of 0.05; dotted line: critical alpha-level after FDR-correction over all tests). (B) Test outcomes over the individual scores of age, cognition, motor function, and sensory task performance. To extract general behavioral features, dimensionality reduction through principal component analysis was applied to individual task performance metrics for the PLS analysis in the main text.

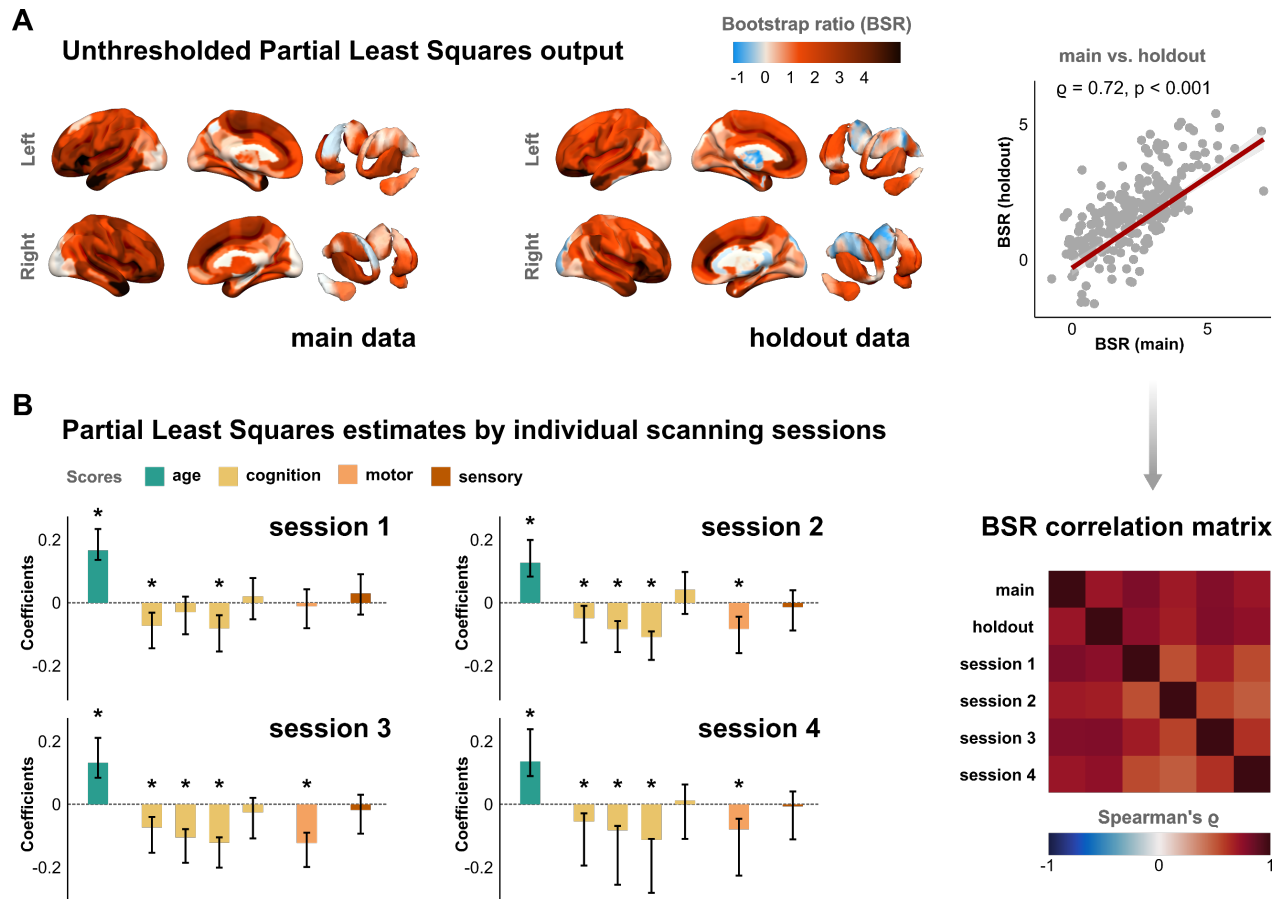
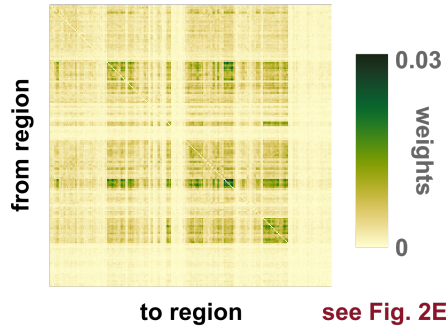


**Fig. S13. Additional Partial Least Squares validation analyses.** (A) Unthresholded maps of the bootstrap ratios (BSR) in Figure 7 for the main and holdout data. Non-parametric correlation of the BSR values in main and holdout dataset. (B) Complexity-behavior effect estimates over each of the four individual scanning sessions. As in Figure 7, error bars correspond to bootstrapped confidence intervals, and asterisks indicate significant effects. The right panel shows the correlation matrix of BSR values over the averaged data in the main and holdout set in Figure 7 as well as for individual scanning sessions.

**Peak threshold = 10 regions \***

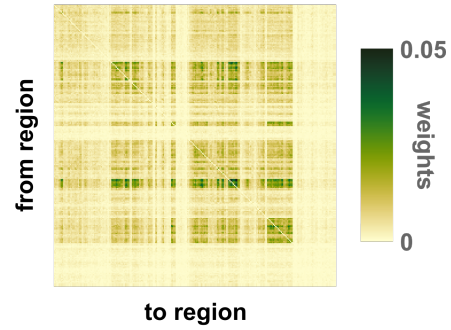
# cascades ~ 5300



see Fig. 2E

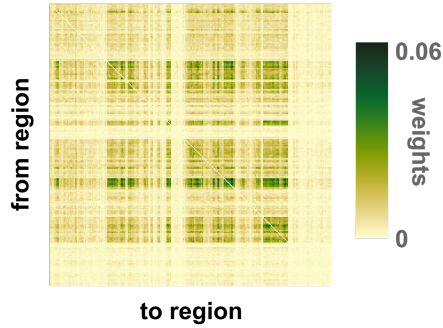
**Peak threshold = 15 regions \***

# cascades ~ 2800



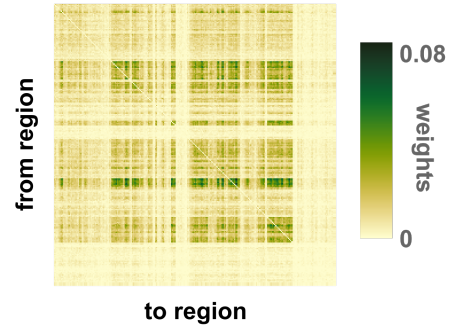
**Peak threshold = 20 regions \***

# cascades ~ 1800



**Peak threshold = 25 regions \***

# cascades ~ 1300



**\* all pairwise correlations:  $\rho \geq 0.94$ ,  $p < 0.001$**

**Fig. S14. Drop propagation networks over different peak thresholds.** Matrices represent the unthresholded transition weights of drop propagations (see Figure 2). Note that these matrices are not perfectly symmetrical, as they encode the temporal direction of the propagations (from rows to columns). Increasing the peak threshold (i.e., the minimum number of regions showing complexity drops in the peak window) results in gradually lower number of cascades in total, as expected. In contrast, the structure of the spatiotemporal propagation pathways is highly consistent across the different peak thresholds. The upper left panel corresponds to the propagation network in Fig. 2E.

**Movie S1. Visualizing complexity drops.** The clip shows the first 50 windows of regional complexity timeseries (cf., Fig. 1A), corresponding to ~2.5 minutes of resting-state fMRI activity from an exemplary recording (participant 22). White indicates high-complexity activity of a given region, while colors indicate moderate (brown) to strong (blue) drops in complexity over the current window. Note the spread of complexity drops to increasingly more regions around window 10 (~1 min) and 40 (~2.1 mins), corresponding to individual drop cascades (Fig. 2A). These spreads are modelled with directed graphs (Fig. 2B) that underlie the reported propagation analyses (Fig. 2C-G).

The movie file is available from <https://osf.io/mr8f7>.